DETACHED-EDDY SIMULATION OF UH-60A AIRLOADS USING AN IMMERSED BOUNDARY METHOD

Jack Heesung Park, The University of Sydney, Sydney, Australia
Daniel Linton, The University of Sydney, Sydney, Australia
Ben Thornber, The University of Sydney, Sydney, Australia

Abstract

The complete helicopter configuration of UH-60A Black Hawk in forward flight is numerically studied using an immersed boundary method and an actuator surface model. Detached-eddy simulation is conducted where the UH-60A fuselage is represented by the immersed boundary method, while the main and tail rotors are modeled using the actuator surface model. The low-speed case (flight counter 8513) from the UH-60A Airloads Program by NASA and the U.S. Army is considered. This case poses challenges such as significant blade-vortex interaction and rotor-airframe interaction. The validation of the test case is conducted for both isolated main rotor and full configurations, and the results are compared with flight test measurements and computational data from the literature. The main rotor blade airload data show excellent agreement with the reference data. The fuselage effect is observed in the inboard stations of the main rotor. The surface pressure data over the centerline of the fuselage, vertical stabilizer, and horizontal stabilator are presented. Qualitative data demonstrate massive flow separation from subcomponents of the fuselage that are often not included in computational fluid dynamics simulations. It also features significant main rotor-tail rotor interactions. The computational effort for three grid levels of each test case is provided.

1. NOTATION

Symbols

C_d	Section drag coefficient
C_l	Section lift coefficient
C_n	Normal force coefficient
C_p	Pressure coefficient
C_T	Rotor thrust coefficient
C_Q	Rotor torque coefficient
c	Chord length, m
L	Fuselage length, m
M	Mach number
p	Pressure (normalized by density), m^2/s^2
$\boldsymbol{p}$	Position vector, m
R	Rotor radius, m
$\boldsymbol{R}$	Reynolds stress tensor
Re	Reynolds number
S	Wing span, m
$\boldsymbol{S}$	Momentum source term, m/s^2
t	Time, s
$\boldsymbol{U}$	Velocity vector, m/s
u^+	Dimensionless velocity
u_τ	Friction velocity, m/s
x, y, z	Spatial coordinates, m
y^+	Dimensionless wall distance
β	Flap angle, deg
$\beta_0, \beta_{1c}, \beta_{1s}$	Coning, longitudinal and lateral blade flapping angles, deg
ζ	Lag angle, deg
$\zeta_0, \zeta_{1c}, \zeta_{1s}$	Mean, first harmonic cosine and sine lag angles, deg
θ	Pitch angle, deg
$\theta_0, \theta_{1c}, \theta_{1s}$	Collective, lateral and longitudinal cyclic pitch angles, deg
μ	Advance ratio
ν	Kinematic viscosity, m^2/s
ν_t	Turbulent viscosity, m^2/s
$\tilde{\nu}$	Pseudo-turbulent viscosity, m^2/s
σ	Solidity
ψ	Azimuth angle, deg

Subscript

b	Induced by bound vorticity of blade
CFD	Quantity sampled from the computational fluid dynamics flow field
g	Relative velocity due to blade motion
h	Horizontal stabilator
ib	Quantity evaluated at immersed boundary cell centroid
in	Induced velocity
m	Main rotor blade
max	Maximum value
min	Minimum value
n	Normal component of quantity
ref	Reference value
s	Time the sampled quantity is taken
sp	Quantity evaluated at sample point
t	Tangential component of quantity or tail rotor blade
tip	Quantity evaluated at advancing blade tip

v	Vertical stabilizer
w	Induced by wake
∞	Freestream value

Superscript

n	Number of iteration
$'$	Fluctuating value

Acronyms:

ASM	Actuator Surface Model
BVI	Blade-Vortex Interaction
CAD	Computer-Aided Design
CSD	Computational Structural Dynamics
CFD	Computational Fluid Dynamics
DDES	Delayed Detached Eddy Simulation
IB	Immersed Boundary
IBM	Immersed Boundary Method
LES	Large Eddy Simulation
PISO	Pressure Implicit with Separation of Operators
PSP	Pressure-Sensitive Paint
RANS	Reynolds-Averaged Navier-Stokes
ROBIN	ROtor Body Interaction
S-A	Spalart-Allmaras
TVD	Total-Variation-Diminishing
WLS	Weighted Least-Squares

2. INTRODUCTION

The flow around a complete helicopter configuration involves a wide variety of complex and interacting physical phenomena. The presence of the airframe distorts the inflow through the rotor disk, and this influences the blade airloads and rotor performance (Ref. 1). Tail rotor operation is also hugely impacted by the presence of the main rotor wake as well as the vertical and horizontal tails (Ref. 1). These effects are very complicated, and it is challenging to predict as the rotor aerodynamics must be modeled using sophisticated and advanced forms of unsteady aerodynamics (Ref. 1). State-of-the-art approaches in this field are high-fidelity computational fluid dynamics (CFD) simulations coupled with a comprehensive rotorcraft analysis code for computational structural dynamics (CSD) analyses (Ref. 2). This integrated approach showed significant improvement in airloads and structural loads predictions compared to when the comprehensive analysis is conducted with simplified rotor inflow and wake modeling (Ref. 3). However, the high-fidelity CFD simulations of the complete rotorcraft configuration are challenging because a significant amount of computational cost and manpower is required to perform such computations. Hybrid Navier-Stokes/rotor aerodynamics models (Ref. 4) as alternatives can predict the performance of the rotor blade with a reasonable level of accuracy at a fraction of the cost compared to the resolved blade, but the fuselage must still be meshed.

Two primary types of grids available are structured and unstructured grids. While the structured grid typically provides better convergence and accuracy over the unstructured grid, generating a structured grid for a complicated fuselage geometry can be extremely difficult and time-consuming (see Ref. 5 for an example). Lakshminarayan et al. (Ref. 6) identified that this disadvantage of the structured grid acts as a barrier for the CFD tool to be used for full rotorcraft simulations. Unstructured grid generation can be more flexible with the geometry and fully automated, but great care must be taken in selecting numerical schemes because of relatively low mesh quality, and the overall computational expense may be higher than the structured grid to achieve an equivalent level of accuracy. A state-of-the-art approach developed to address those issues is the strand mesh (Ref. 7). This grid consists of prism cells that are produced by inflating the surface grid of the body. The strand mesh not only enables fully automated grid generation but also possesses a grid structure similar to Cartesian mesh, allowing high-order accurate numerical schemes and efficient data exchange (Ref. 6).

The proposed method for the fuselage mesh in this study is the immersed boundary method (IBM). The IBM is a non-body conformal mesh approach that represents an object of interest in the flow using a momentum forcing in the Navier-Stokes equation to enforce the wall boundary condition onto the flow field. This method employs simple Cartesian grids, which enable fully automated meshing of complicated geometries. Park et al. (Refs. 8–10) developed an IBM solver and integrated it with an actuator surface model (ASM), which was developed by Linton et al. (Refs. 4, 11). The ASM is based on the rotor aerodynamics model coupled with the CFD solution and uses the momentum source to represent unsteady rotors. This coupled approach has been successfully demonstrated for complete helicopter configurations with generic fuselage geometries, including Georgia Institute of Technology rotor-airframe (Ref. 8) and the ROtor Body INteraction (ROBIN) mod 7 fuselage with pressure-sensitive paint (PSP) rotor (Ref. 10). The IBM used in this research is based on the discrete forcing approach, which employs Reynolds-averaged Navier-Stokes (RANS) turbulence model and a turbulent wall function for high Reynolds number flow simulations.

The UH-60A Airloads Program by NASA and the U.S. Army (Ref. 12) produced an extensive flight test dataset for hover, level flight, and maneuvering flight conditions. The most intensively studied flight conditions using numerical methods are flight counters 8513 (C8513), 8534 (C8534), and 9017 (C9017); they are characterized by their low-speed, high-speed, and high-thrust conditions, respectively. The full flight test data for those flight conditions are available in Refs. 13–15. The full configuration was numerically studied for the high-speed condition using the CFD/CSD coupled approach by Biedron and Lee-Rausch (Ref. 16) and Lakshminarayan et al. (Ref. 6). While the number of studies on the full configuration is limited, there have been numerous publications on the isolated main rotor in forward flight using the following methods: comprehensive analysis codes (Refs. 3, 17, 18), CFD codes (Refs. 4, 19), and hybrids of the two (Refs. 3, 20–28).

In this study, the low-speed forward flight condition is studied on both isolated main rotor and full configurations. The fuselage is represented by the IBM, and the main and tail rotors are modeled using the ASM. This case poses challenges such as significant blade-vortex interaction (BVI) and rotor-airframe interaction. The blade airload data are measured from both isolated main rotor and rotor-fuselage cases. The fuselage effect is analyzed in both quantitative and qualitative manners. The surface pressure distribution over the fuselage is investigated. Each test case is validated against both flight test and numerical data from the literature.

This paper is structured as follows: the numerical methods section describes each component of the underlying numerical method; the computational setup section details the computational setup of the test cases including geometrical parameters, rotor blade operating conditions, and computational grids; the results and discussion section provides simulation results with discussion; the computational metrics section presents the computational effort for each test condition; the conclusions section offers a summary of this research.

3. NUMERICAL METHODS

This section describes the governing equations, turbulence modeling, and each component of the IBM-ASM solver. Numerical schemes and Navier-Stokes solvers are also detailed.

3.1. Governing equations

The incompressible RANS equations are solved, which are

$$\frac{\partial\langle \boldsymbol{U}\rangle}{\partial t} + (\langle \boldsymbol{U}\rangle \cdot \nabla)\langle \boldsymbol{U}\rangle = -\nabla\langle p\rangle + \nabla\cdot(\nu\nabla\langle \boldsymbol{U}\rangle + \boldsymbol{R}) + \boldsymbol{S} \tag{1}$$

$$\nabla\cdot\langle \boldsymbol{U}\rangle = 0 \tag{2}$$

where $\boldsymbol{U}$ is the velocity vector, and it is decomposed into time-averaged and fluctuating components $\boldsymbol{U} = \langle \boldsymbol{U}\rangle + \boldsymbol{U}'$; p is the pressure normalized by density; ν is the kinematic viscosity; $\boldsymbol{R} = -\langle \boldsymbol{U}' \otimes \boldsymbol{U}'\rangle$ represents the Reynolds stress tensor; $\boldsymbol{S}$ is the momentum source term.

In this study, delayed detached eddy simulation (DDES) of Spalart et al. (Ref. 29) is used for all cases. The rotor wake flow in the presence of the fuselage involves complicated flow characteristics, such as the turbulent rotor wake interacting with the fuselage boundary layer and its separated wake. The hybrid method between RANS and large eddy simulation (LES) is employed in the present study to minimize computational cost for resolving the boundary layer but accurately capture the highly turbulent wake due to the flow separation from the fuselage and its interaction with the rotor wake.

3.2. Immersed boundary method

The IBM used in this investigation has its basis on the discrete forcing approach of Jasak et al. (Ref. 30). They utilized the multi-variable quadratic interpolation with the weighted least-squares (WLS) method for fluid quantities to be interpolated to immersed boundary (IB) cell centroids. Park et al. (Ref. 8) adopted this method and developed their IBM solver by implementing the Spalart-Allmaras (S-A) analytical wall model (Refs. 31, 32). Park et al. (Ref. 9) further improved the wall function to enhance the solver accuracy; the geometric cut-off criterion ($y < y_{sp}$) to determine the boundary layer modeling region was switched to the flow-based cut-off criterion ($y^+ < y^+_{sp}$); a WLS gradient numerical scheme was implemented; a multi-grid refinement level functionality was added, which allowed different grid spacings across the wall. The following briefly describes the turbulent wall function, and the schematic of the IBM with the wall function is illustrated in Figure 1.

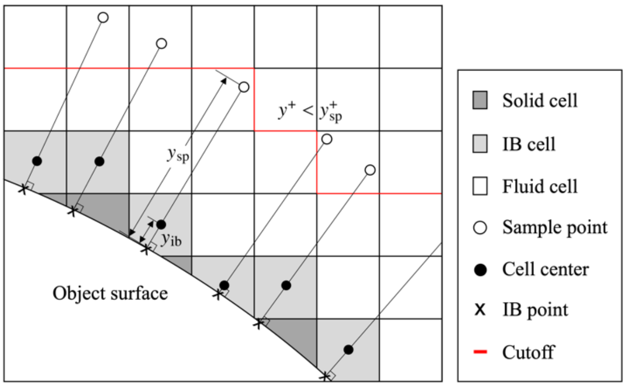

Figure 1: Schematic of the IBM with the wall function.

The wall function uses sample points (represented by the subscript "sp") as reference points to obtain fluid quantities. The sample offset from the IB surface is fixed at $y_{sp} = 3\Delta x$ for two-dimensional (2-D) cases or $2\Delta x$ for three-dimensional (3-D) cases, where Δx is the local grid spacing. This local grid spacing may vary if the multi-grid refinement level functionality is employed. A different value may also be utilized for the constant parameter in the sample offset, though note that the sample points need to be located far enough from the IB surface to have enough fluid cells for interpolation but close enough to the surface to be within the boundary layer (Ref. 8).

The tangential velocity $u_{ib,t}$ (the subscript "ib" denotes that the value is evaluated at the centroid of the IB cells) is computed by

$$u_{ib,t} = u_{sp,t} - \left\{\frac{\partial u^+}{\partial y^+}\left(y^+_{sp}\right)\right\}\left(y^+_{sp} - y^+_{ib}\right)u_\tau \tag{3}$$

where the velocity gradient $\partial u^+/\partial y^+$ with respect to the wall unit y^+_{sp} can be obtained from the S-A analytical wall model (Refs. 31, 32), and the friction velocity u_τ can be calculated using the Newton-Raphson method

$$u_\tau^{n+1} = u_\tau^n - \frac{f(u_\tau^n)}{f'(u_\tau^n)} \tag{4}$$

with the function f and its derivative defined as

$$\begin{aligned} f(u_\tau) &= u_\tau u^+\left(y^+_{sp}\right) - u_{sp,t} \\ f'(u_\tau) &= u^+\left(y^+_{sp}\right) + u_\tau \frac{\partial u^+}{\partial u_\tau}\left(y^+_{sp}\right) \end{aligned} \tag{5}$$

The normal velocity $u_{ib,n}$ can be obtained by applying the non-penetrating condition at the wall

$$u_{ib,n} = \frac{y_{ib}}{y_{sp}} u_{sp,n} \tag{6}$$

where y is the wall distance. On the other hand, the pressure p_{ib} is obtained using the multi-variable quadratic interpolation method of Jasak et al. (Ref. 30).

The S-A turbulence model is formulated to have a linear solution for the pseudo-turbulent viscosity $\tilde{\nu}$ in the boundary layer. Therefore, $\tilde{\nu}_{ib}$ is computed by

$$\tilde{\nu}_{ib} = \kappa u_\tau y_{ib}, \qquad \kappa = 0.41 \tag{7}$$

Lastly, the turbulent viscosity $\nu_t = \tilde{\nu} f_{v1}$ is calculated using the modified S-A damping function f'_{v1} (see Ref. 32 for details).

3.3. Actuator surface model

In this section, the ASM solver used in the present study is briefly explained, and an interested reader can consult Refs. 4, 11 for the description and validation.

The underlying method is composed of two main components: the rotor aerodynamics model based on the lifting-line theory and the CFD-rotor model coupling method (Refs. 4, 11). In the rotor aerodynamics model, a 2-D aerodynamics coefficient table is used to determine the spanwise loading distribution for the blade that is projected back onto the CFD solution through the momentum source term field $\boldsymbol{S}$ in Eq. (1). The unsteady modeling of Beddoes (Ref. 33) is used in conjunction with tabulated section lift and drag coefficients (C_l and C_d, respectively) of 2-D airfoils. Also, sweep/yawed flow corrections are also performed to account for the flow in the spanwise direction, and this method is taken from Johnson (Ref. 34).

The ASM employs a two-way coupling of the CFD solver and rotor model. The induced velocity $\boldsymbol{U}_{in}$ is calculated utilizing the CFD solution and passed to the rotor model to calculate the parameters mentioned above. The complete expression for $\boldsymbol{U}_{in}$ at time t is (Ref. 4)

$$\boldsymbol{U}_{in} = \boldsymbol{U}_g(\boldsymbol{p}_c, t) + \boldsymbol{U}_{CFD}(\boldsymbol{p}_s, t_s) + \boldsymbol{U}_{in,w}(\boldsymbol{p}_c, t) - \boldsymbol{U}_{in,w}(\boldsymbol{p}_s, t_s) - \boldsymbol{U}_{in,b}(\boldsymbol{p}_s, t_s) \quad (8)$$

In the preceding equation, the terms with $\boldsymbol{p}_c$ are evaluated at the collocation point on the blade, which is at the 3/4-chord point on each spanwise panel; the terms involving $\boldsymbol{p}_s$ are evaluated at the sample point which is located one chord length ahead of the blade section; t_s indicates the time the sampled velocity is taken. The geometric velocity $\boldsymbol{U}_g$ is the velocity of the blade relative to the global reference frame of the computational domain; the sampled velocity $\boldsymbol{U}_{CFD}$ is extracted from the CFD solution at the sample point, and it is corrected considering the delay between the sample being taken (t_s) and the blade reaching the sample point (t); the induced velocity due to the wake $\boldsymbol{U}_{in,w}$ is the difference of the downwash and wake correction calculated from the CFD-convected wake model; the bound vorticity correction $\boldsymbol{U}_{in,b}$ is computed using a vortex core model of Ramasamy and Leishman (Ref. 35) to avoid singularities. Lastly, the spanwise loading distribution from the rotor model is then converted to the momentum source field onto the discrete CFD grid. The chord normal distribution uses a Gaussian function, whereas the chordwise function is adopted from Kim et al. (Ref. 36).

The coupling with the IBM solver is straightforward with no modifications required to either model for them to work together in one computation. The open-source Navier-Stokes CFD suite OpenFOAM (Ref. 37) is used for the present implementation, which provides a framework for the development of customized numerical solvers, turbulence models, and turbulent wall functions. In the OpenFOAM framework, the ASM library can be utilized as a momentum source model for $\boldsymbol{S}$ in Eq. (1).

3.4. Numerical scheme and solver

A hybrid numerical scheme of Spalart et al. (Ref. 38) is utilized for the convective terms; a second-order centered scheme is used in the LES region, and a second-order total-variation-diminishing (TVD) scheme with the limited linear flux limiter (Ref. 37) is employed in the RANS region. The use of the TVD scheme is to ensure the flow over IB surfaces that are not aligned with mesh layers to remain realistic by maintaining monotonicity in the convection of momentum. The second-order centered scheme is also utilized for non-convective terms, and a second-order implicit scheme is applied to temporal discretization. A segregated solver of the pressure implicit with separation of operators (PISO) algorithm (Ref. 39) is used to resolve the pressure-velocity coupling in all calculations.

4. COMPUTATIONAL SETUP

In this section, details of the fuselage and rotor geometries, flow conditions, rotor operating conditions, and computational grids are given.

4.1. Fuselage geometry and flow conditions

The fuselage geometry is designed following reference parameters provided in Refs. 40–42. The fuselage length L is 15.1m, which is slightly shorter than the reference length 15.4m. The vertical stabilizer consists of the NACA0021 airfoil with the sweep angle of 41 deg. The horizontal stabiliator is made up of the NACA0014 airfoil, and its pitch angle can vary from -8 deg to 39 deg depending on the operating conditions of the rotorcraft (Ref. 42). In Table 1, the pitch and roll attitudes, and sideslip angle of the fuselage, the incidence angle of the horizontal stabilator, and parameters indicating the flow condition in terms of the fuselage is summarized.

Table 1: Parameters for the fuselage.

Parameter	Value
Pitch attitude, deg	3.37
Roll attitude, deg	-4.64
Sideslip angle, deg	2.85
Stabilator pitch angle, deg	17.2
Freestream velocity U_∞, m/s	33.4
Freestream Mach number M_∞	0.096
Reynolds number Re_L ($\times 10^6$)	31.2

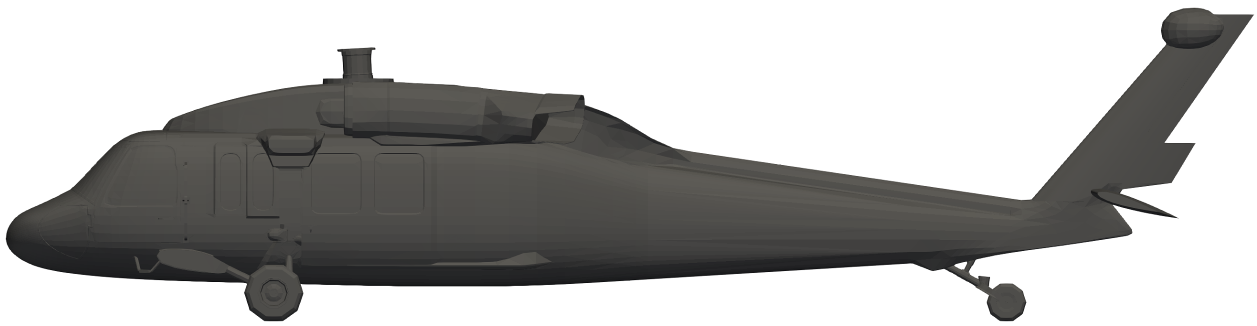

Figure 2: UH-60A fuselage geometry.

The parameters are obtained from the flight test data (Ref. 13). Note that the angle of attack of the fuselage is ignored, as there is a possibility that the downwash was taken into account for the data in the flight test. The table uses the positive sign convention as follows: nose up (leading edge up) for the pitch angle, roll right for the roll angle, and nose left for the sideslip angle. The freestream velocity U_∞ is 33.4m/s, and this leads the freestream Mach number M_∞ and the Reynolds number based on the fuselage length Re_L to be 0.233 and 76.0×10^6, respectively. In this study, most of geometrical details, such as the engine intake and exhaust, doors, struts, and wheels, are retained to make the fuselage geometry as close as to the “true” configuration as possible. This is to accurately capture the flow separation from every component of the fuselage. A computer-aided design (CAD) model of the fuselage geometry is presented in Figure 2.

Table 2: Parameters for the main and tail rotor blades.

Parameter	Main rotor	Tail rotor
Rotor radius R, m	8.1778	1.6764
Root cutout	13%R	10%R
Number of blades	4	4
Solidity σ	0.0826	0.1875
Lock number	8.1936	3.3783
Reference chord c_{ref}, m	0.5273	0.2469
Tip sweep, deg	20 at 93%R	–
Linear twist, deg/R	-16	-18
Rotor shaft speed, rpm	258	1190
Rotor shaft angle, deg	3	–
Precone angle, deg	–	0.75
Cant angle, deg	–	20
Hub stationline, inches	341.2	732.0
Hub waterline, inches	315.0	324.7
Hub buttline, inches	–	14

4.2. Rotor geometry and operating conditions

The geometric parameters for the main and tail rotor blades are given in Table 2. The table is mainly based on Refs. 41–43. The geometry of the main rotor blade follows the one used by Linton et al. (Ref. 4). It is taken from the wind-tunnel-model geometry of Lorber et al. (Ref. 44). The main rotor radius R_m is 8.1778m. The airfoil profiles are SC1095 inboard from 0.47 R_m , SC1094-R8 to 0.82R_m, and SC1095 out to the tip. The equivalent linear twist for the blade is -16 deg with a nonlinear twist used at the tip. The constant chord length is used for the entire blade. The trim tab on the full-scale blade (Ref. 43) has been ignored for simplicity; the aerodynamic effect of the trim tab on the rotor blade was found to be small by Chaderjian and Ahmad (Ref. 26). The sweep angle at the tip of the blade is 20 deg for the final 7% of the span. The rotor shaft angle is 3 deg. The planform of the blade is illustrated in Figure 3.

The geometry of the tail rotor blade is obtained from Hilbert (Ref. 42). The tail rotor radius R_t is 1.6764m.

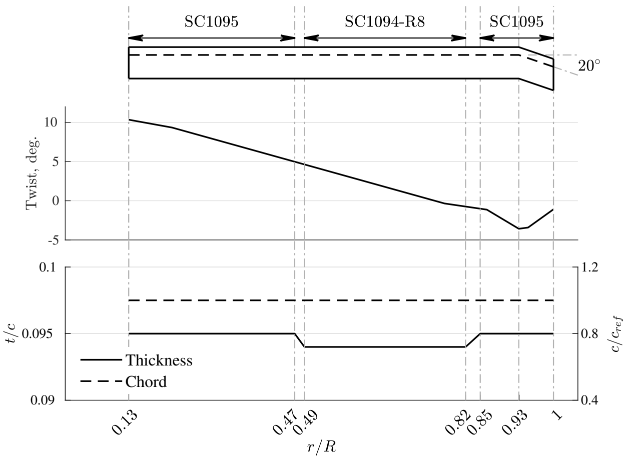

Figure 3: Geometry of the UH-60A main rotor blade reproduced from Linton et al. (Ref. 4).

Table 3: Flight condition and control settings for the main rotor blade.

Parameter	C_T/σ	μ	M_{tip}	θ_0	θ_{1c}	θ_{1s}	β_0	β_{1c}	β_{1s}	ζ_0	ζ_{1c}	ζ_{1s}
Value	0.0792	0.151	0.743	5.18	2.91	-4.36	2.74	1.74	0.42	-3.32	0.29	-0.12

The blade is comprised of the SC1095 airfoil with the constant chord for the entire blade. Its root cut-out is arbitrarily set as $0.1R$ as this property is not given in the literature. The blade is twisted at -18 deg and canted at 20 deg. The blade flap-pitch coupling by "delta-3" hinge is not considered. The pre-cone angle of 0.75 deg is included in the flap motion of the blade.

The flight condition and control settings for the main rotor blade are provided in Table 3. In the table, C_T/σ is the solidity-weighted thrust coefficient; μ represents the advance ratio; M_{tip} denotes the advancing tip Mach number. The periodic motion of the flap hinge β, lead/lag hinge ζ, and pitch bearing θ are described using the Fourier series as a function of the azimuth angle ψ

$$\begin{aligned} \beta(\psi) &= \beta_0 + \beta_{1c}cos(\psi) + \beta_{1s}sin(\psi) \\ \zeta(\psi) &= \zeta_0 + \zeta_{1c}cos(\psi) + \zeta_{1s}sin(\psi) \\ \theta(\psi) &= \theta_0 + \theta_{1c}cos(\psi) + \theta_{1s}sin(\psi) \end{aligned} \quad (9)$$

In the preceding equation, β_0 denotes the coning angle; β_{1c} and β_{1s} are the longitudinal and lateral blade flapping angles, respectively; ζ_0 represents the mean lag angle; ζ_{1c} and ζ_{1s} are first harmonic cosine and sine lag angles, respectively; θ_0 corresponds to the collective pitch angle; θ_{1c} and θ_{1s} are lateral and longitudinal cyclic pitch angles, respectively. The values of these coefficients given in Table 3 are obtained from the flight test data (Ref. 13) except for θ_0; the isolated main rotor is trimmed for the thrust using the given coefficients to determine θ_0. For the tail rotor, the thrust for the canted rotor is calculated to balance the main rotor torque, then the isolated tail rotor is trimmed for the thrust to obtain its collective pitch.

The boundary layer is modeled fully turbulent, and the boundary layer transition is not considered. Aerodynamic coefficient tables for the airfoils are obtained utilizing Xfoil (Ref. 45), which is an open-source code that uses a panel method with compressibility correction. Viterna and Corrigan's simple poststall model (Ref. 46) is employed to extend the polars to $\pm$180 deg.

Table 4: Grid specification.

Grid	Δx_{min}, ($\times10^{-3}$) m	$y^+_{sp,max}$	Cell count, ($\times10^6$) cells
Isolated rotor			
Coarse	85.19	–	4.6
Medium	58.97	–	13.5
Fine	42.59	–	35.7
Rotor-fuselage			
Coarse	2.66	920	146.7
Medium	1.84	673	309.4
Fine	1.33	521	603.0

4.3. Computational grid

The grid is divided into seven regions. The main rotor region is a cylinder of radius $1.1R_m$, and it extends from $0.2R_m$ above to $0.25R_m$ below the rotor plane. The main rotor near-wake and far-wake regions are cuboids; the dimensions of the former are [$-1.1R_m$, $5R_m$] × [$-1.5R_m$, $1.5R_m$] × [$-R_m$, $0.3R_m$]; those of the latter are [$-1.1R_m$, $7R_m$] × [$-1.75R_m$, $1.75R_m$] × [$-1.5R_m$, $0.5R_m$] in x, y, and z directions, respectively. The horizontal stabilator region is also a cuboid, and its dimensions are determined based on the size of the wake region in preliminary calculations. The tail rotor region is another cylinder of radius $1.1R_t$, and it extends from $0.7R_t$ above to $0.7R_t$ below the disk. The sixth region is the fuselage near-wall region, which is obtained using local grid refinement across the surface of the fuselage. Lastly, the background mesh is composed to have the outflow boundary located $12R_m$ from the hub and all other boundaries located $6R_m$ from the hub.

Three grid levels are used for the grid convergence test. Details of the grids are provided in Table 4. The grid is refined by an arbitrary amount that doubles the cell count as the grid level increases. The refinement factor between grid levels can be calculated from the minimum grid spacing Δx_{min} in the table. $y^+_{sp,max}$ is the maximum value of dimensionless distances from the wall at sample points, and it indicates the grid resolution in the near-wall region.

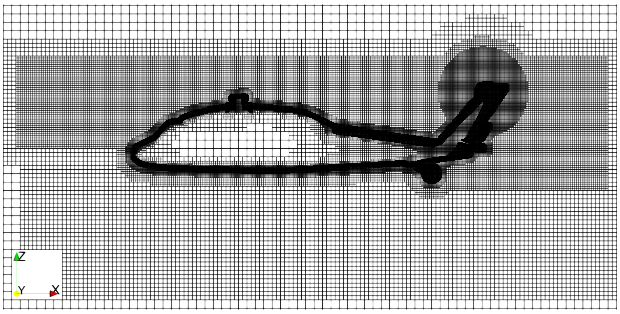

Figure 4: y-normal slice of the computational mesh. A close-up around the fuselage.

From the medium grid level, the grid spacings in the main and tail rotor regions are below 0.15c_{ref} of the respective blades, where c_{ref} denotes the reference chord length; this value is recommended by Linton et al. (Ref. 4). For the isolated rotor case, the fuselage near-wall region is not refined. The resulting number of cells in the coarse, medium, and fine grids are 4.6×10^6, 13.5×10^6, and 35.7×10^6, respectively. The local grid refinement is carried out in the near-wall region for the rotor-fuselage case, and the cell counts for the coarse, medium, and fine grids are 146.7×10^6, 309.4×10^6, and 603.0×10^6, respectively. For the boundary conditions, the velocity inlet, pressure outlet, and freestream side boundaries are applied; the freestream boundary conditions followed guidelines from Ref. 47. A close-up of the fine grid around the fuselage is presented in Figure 4.

5. RESULTS AND DISCUSSION

This section presents the simulation results, and they are discussed and compared with reference data from the literature.

Table 5: Solidity-weighted thrust and torque coefficients.

Study	C_T/σ	C_Q/σ
Flight test (Ref. 13)	0.0792	0.0041
Isolated rotor		
Coarse	0.0797	0.00353
Medium	0.0797	0.00353
Fine	0.0797	0.00352
Rotor-fuselage		
Coarse	0.0792	0.00346
Medium	0.0791	0.00345
Fine	0.0791	0.00345

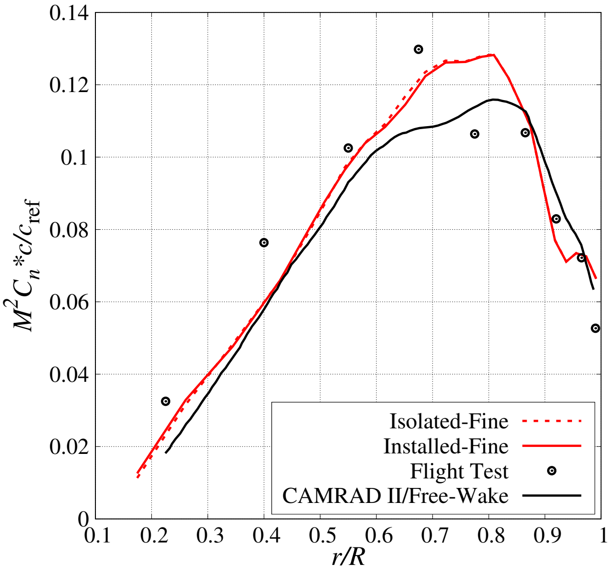

Figure 5: Mean normal force distribution with the flight test data from Ref. 13 and CAMRAD II/free-wake data from Ref. 3.

5.1. Blade airloads

Table 5 shows the solidity-weighted thrust and torque coefficients (C_T/σ and C_Q/σ, respectively) from the simulation results, and they are compared with the flight test data (Ref. 13). The simulation results demonstrate good grid convergence. The thrust from the rotor-fuselage case has excellent agreement with the flight test data, while the torque is underpredicted (maximum 15.9% difference).

The Mach-weighted normal force coefficient M^2C_n is measured from the simulations for blade airload comparisons with the reference data. The comparisons are made in a normalized fashion by removing the mean value, plotted in Figure 5, because of uncertainty in the flight test data (Refs. 3, 12). In Figure 5, the results from the fine grids of both isolated rotor and rotor-fuselage cases are compared with data from the flight test and a comprehensive analysis code CAMRAD II using a free wake model (Ref. 3). The results are in good agreement with the reference data, accurately capturing the peak at $r/R =$ 0.675, although it made overprediction at $r/R =$ 0.775 by 19.5% compared to the flight test data.

Figure 6 presents M^2C_n as a function of ψ at six different radial stations on the main rotor blade. The results are compared with data from the flight test, fully resolved unsteady RANS using OVERFLOW coupled with CAMRAD II (Ref. 22), and CAMRAD II with the free-wake model (Ref. 3).

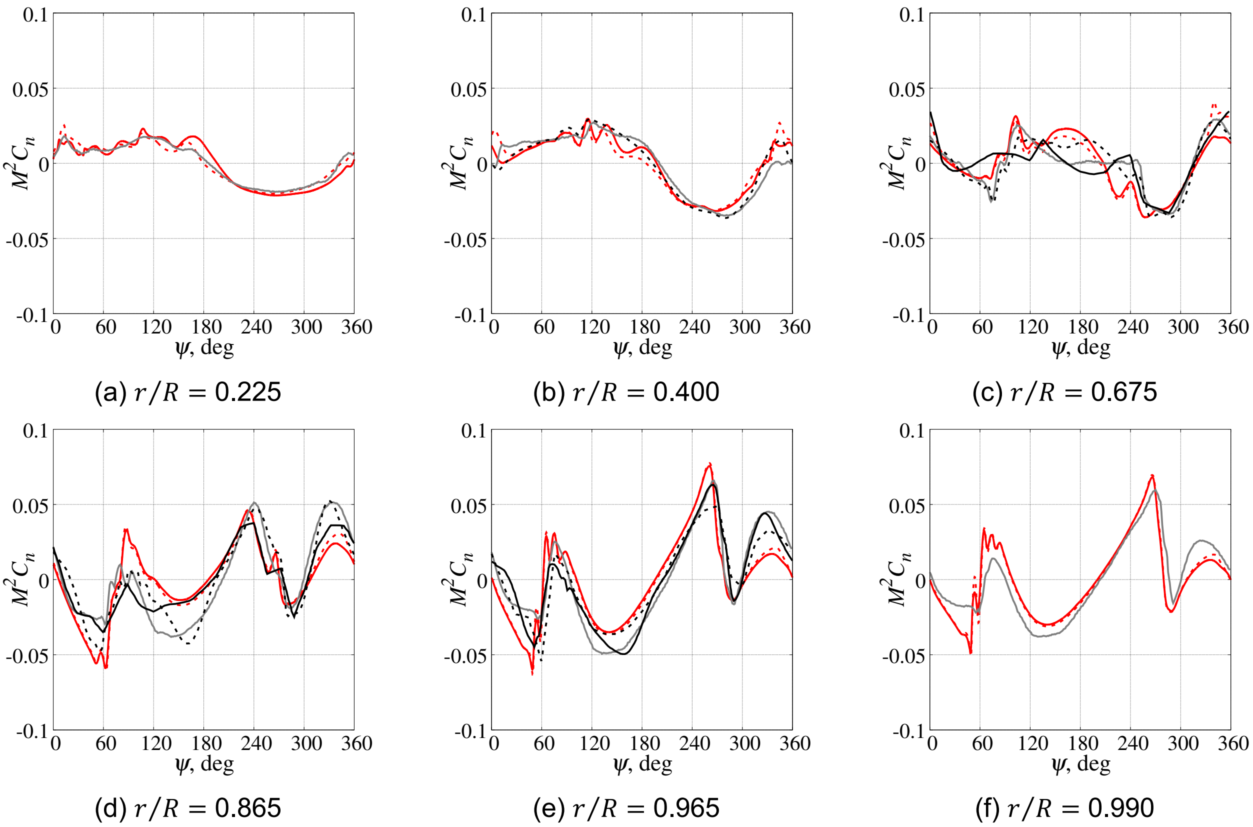

(a) $r/R = 0.225$ (b) $r/R = 0.400$ (c) $r/R = 0.675$

(d) $r/R = 0.865$ (e) $r/R = 0.965$ (f) $r/R = 0.990$

Figure 6: Mach-weighted normal force (mean removed) as a function of azimuth angle at six different radial stations on the main rotor blade. Isolated rotor (···); rotor-fuselage (–); flight test data from Ref. 13 (–); OVERFLOW/CAMRAD II data from Ref. 22 (···); CAMRAD II/free-wake data from Ref. 3 (–).

Overall, the results have good agreement with the flight test data. The sharp variations at $\psi = 90$ and 270 degrees due to BVIs are accurately captured, although there are some discrepancies in magnitude. The results have better agreement with the numerical data than with the flight test data at $r/R =$ 0.675 and 0.865 around the front of the rotor. The fuselage effect can be mainly found in the inboard stations of the rotor, where they are influenced by the fuselage-induced upwash.

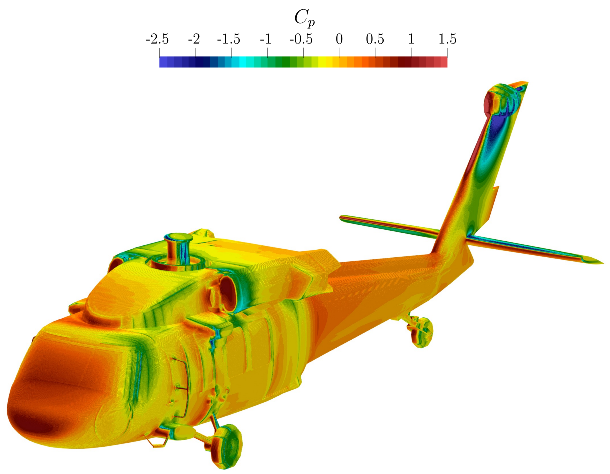

Figure 7: Mean surface pressure distribution over the fuselage (IB cell centroid data).

5.2. Surface pressure over the fuselage

The time-averaged surface pressure coefficient C_p distribution over the fuselage is presented in Figure 7. In Figure 8, the C_p distributions over the top and bottom centerlines of the fuselage are plotted. The results from the three grid levels show excellent grid convergence. Note that C_p over the main rotor hub around $x/L = 0$ is excluded from the figure. The C_p distributions over the chord lines of the horizontal stabilator and vertical stabilizer are provided in Figures 9 and 10, respectively. Here, S_h and S_v denote the spans of the horizontal stabilator and the vertical stabilizer, respectively. The stations are selected arbitrarily, as no reference datasets are available in the literature for comparison. The asymmetry in C_p between the starboard and port sides of the horizontal stabilator is due to the sideslip angle of the fuselage. The tail rotor-vertical stabilizer interaction is found negligible as the tail rotor wake is convected downstream quickly.

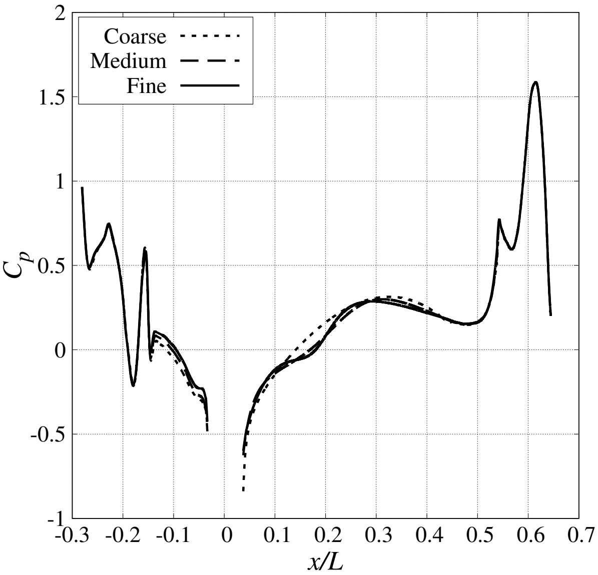

(a) Top centerline.

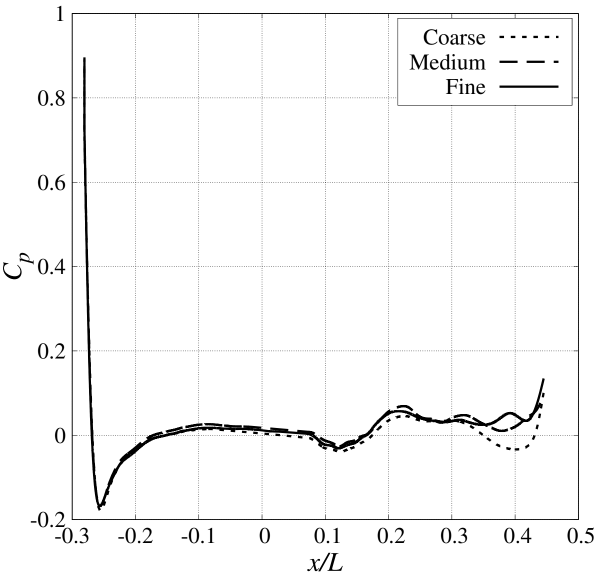

(b) Bottom centerline.

Figure 8: Time-averaged surface pressure coefficient distributions over the top and bottom centerlines of the fuselage.

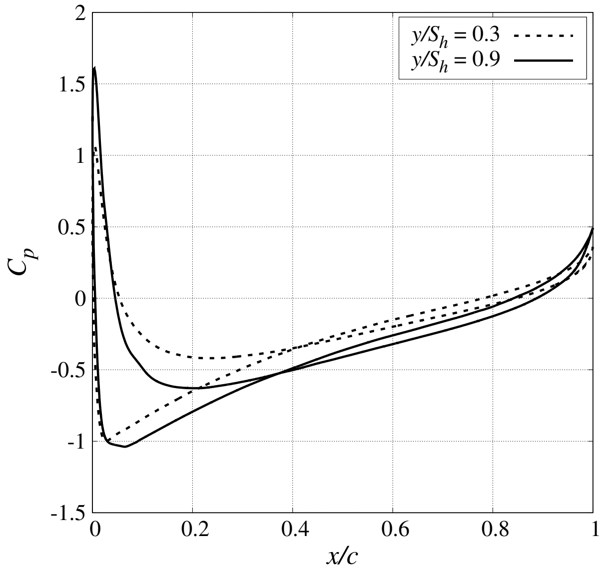

(a) $y > 0$.

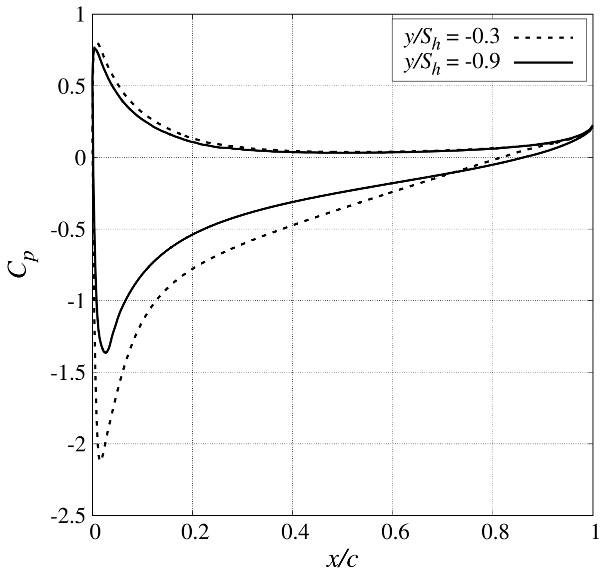

(b) $y < 0$.

Figure 9: Time-averaged surface pressure coefficient distributions over the chord line of the horizontal stabilator. $y/S_h = \pm 0.3$ (–); $y/S_h = \pm 0.9$ (···).

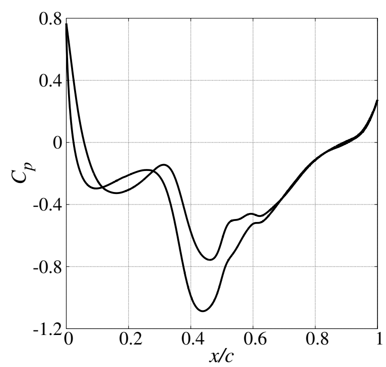

(a) $z/S_v = 0.088$

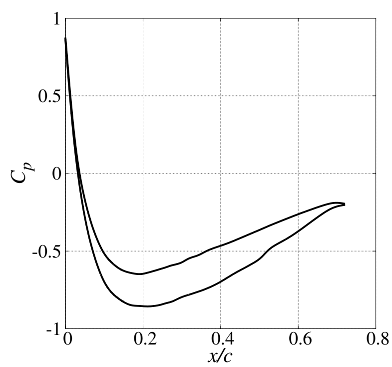

(b) $z/S_v = 0.446$

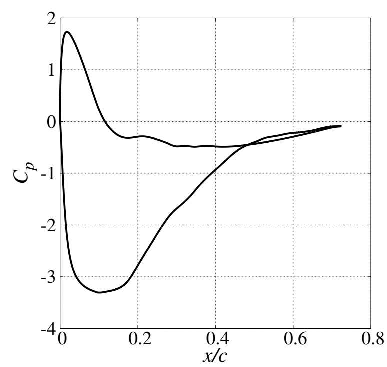

(c) $z/S_v = 0.803$

Figure 10: Time-averaged surface pressure coefficient distributions over the chord line of the vertical stabilizer.

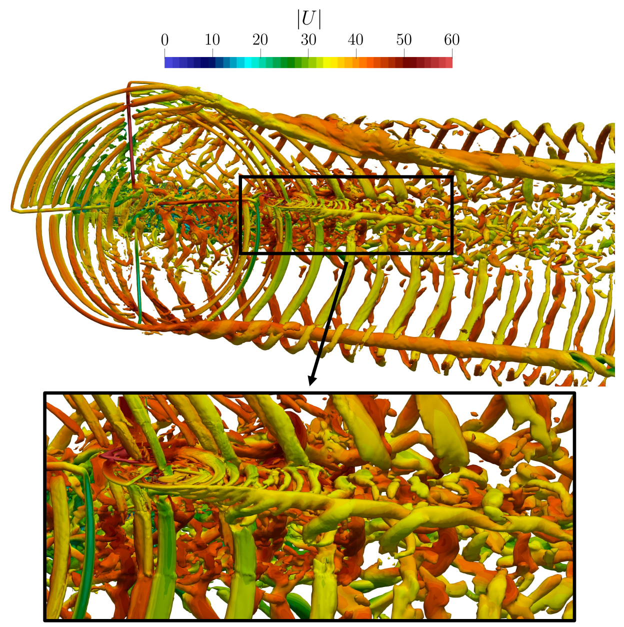

Figure 11: Top view of an instantaneous isosurface of Q criterion ($Q = 150\,\mathrm{s}^{-2}$) colored by the velocity magnitude from the fine grid result of the rotor-fuselage case. A close-up view of the tail rotor wake shows its interaction with the main rotor wake.

5.3. Wake visualization

Figure 11 shows the top view of an instantaneous isosurface of the Q criterion ($Q = 150\,\mathrm{s}^{-2}$) with a close-up view of the tail rotor wake. This is from the fine grid result of the rotor-fuselage case, and the isosurface is colored by the velocity magnitude. It demonstrates significant BVI on the main rotor and main rotor-tail rotor interaction. In Figure 12, the isometric and front views of the isosurface. They feature massively separated wakes from the fuselage and their interaction with the main rotor wake. The flow separation mainly occurred from the engine intake, handlebars, and wheels of the fuselage. These are subcomponents of the fuselage that are often not included in CFD simulations. This implies that this huge flow separation may not have been captured properly in previous studies (Refs. 6, 16).

6. COMPUTATIONAL METRICS

In this section, the computational metrics of the simulations conducted in this study are presented. This section does not discuss the setup cost because the fully automated meshing process using hexahedral meshes is quick (from three hours for the coarse rotor-fuselage grid to twelve hours for the fine grid) and does not require tailoring work. The computational expenses for the three grid levels of both isolated rotor and rotor-fuselage cases are summarized in Table 6. All cases were run on two 64-core AMD Milan 2.45GHz processors per node. The timestep size is based on the main rotor shaft speed. When the ASM is used alone, the computational cost of 24.66, 100.74, and 300.37 core-hours were spent for each revolution for the coarse, medium, and fine grids, respectively. On the other hand, when both the IBM and ASM are used, the computational expenses of 6,874.88, 19,881.19, and 49,583.41 core-hours were spent for each revolution for the coarse, medium, and fine grids, respectively.

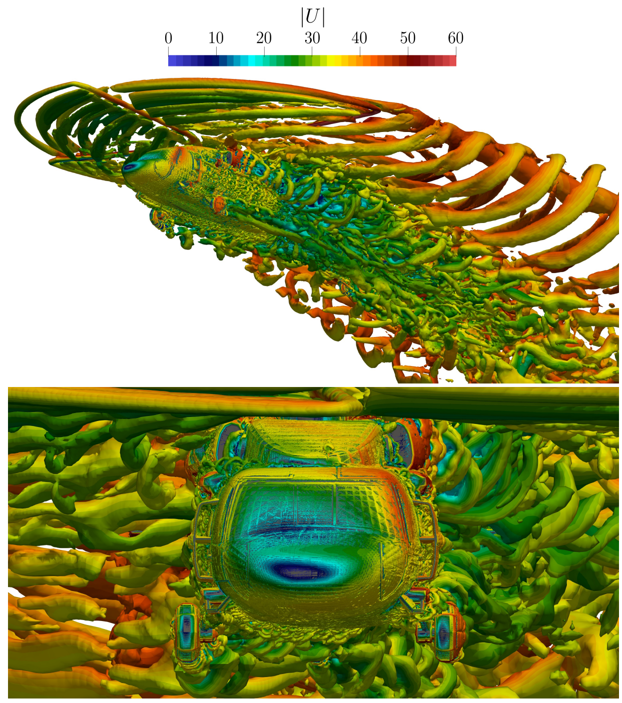

Figure 12: Instantaneous isosurfaces of Q criterion ($Q = 150\mathrm{s}^{-2}$) colored by the velocity magnitude from the fine grid result of the rotor-fuselage case. Isometric view (top) and front view (bottom).

Table 6: Computational effort for all cases.

Grid	Cell count, ($\times 10^6$) cells	Δt, deg/step	Cores	Core-hours/rev
Isolated rotor				
Coarse	4.6	0.5	256	24.66
Medium	13.5	0.5	512	100.74
Fine	35.7	0.5	768	300.37
Rotor-fuselage				
Coarse	146.7	0.12	1,536	6,874.88
Medium	309.4	0.09	3,200	19,881.19
Fine	603.0	0.08	6,400	49,583.41

7. CONCLUSIONS

The UH-60A helicopter configuration has been studied using the IBM-ASM solver. The thrust and torque data showed that the simulation results were fully converged, and the thrust was in excellent agreement with the flight test data. The normal force data have been compared with the flight test and computational data in a normalized fashion by removing the mean value. The mean normal force data had good agreement with the reference data and accurately captured the peak at $r/R = 0.675$. The normal force data at six different radial stations on the main rotor blade also agreed well with the reference data, capturing sharp impulses from BVIs. Fuselage effects were observed in the inboard stations of the main rotor mainly due to the fuselage-induced upwash. The surface pressure data over the top and bottom centerlines of the fuselage demonstrated excellent grid convergence of the simulation results. The surface pressure data over the chord line of the vertical stabilizer showed that there is negligible tail rotor-vertical stabilizer interaction. This is because the tail rotor wake is quickly convected downstream, as observed from the wake visualizations using the Q criterion. The qualitative inspection also showed significant BVI and main rotor-tail rotor interaction, as well as huge flow separation from subcomponents of the fuselage and its interaction with the main rotor wake. These subcomponents have often been ignored in previous numerical studies; thus, the massively separated wake may not have been properly captured before. The computational effort for the three grid levels of both isolated rotor and rotor-fuselage simulations is provided. Future work may include simulations on high-speed and high-thrust conditions.

Author contact:

Ben Thornber ben.thornber@sydney.edu.au

8. ACKNOWLEDGMENTS

The authors acknowledge the computational resources at the National Computational Infrastructure provided through the National Computational Merit Allocation Scheme, as well as the Sydney Informatics Hub and the University of Sydney's high-performance computing cluster Artemis, which were employed for all cases presented here.

9. REFERENCES

1. Leishman, J. G., *Principles of Helicopter Aerodynamics*, 2nd ed., Cambridge University Press, New York, NY, 2006, Chapter 11.

2. Marcolini, M. A., Johnson, W., and Yamauchi, G. K., "Aeromechanics," *A Summary of NASA Rotary Wing Research: Circa 2008-2018*, edited by G. K. Yamauchi, Chap. 2, NASA TP 2019-220459, 2019, pp. 55–120.

3. Potsdam, M., Yeo, H., and Johnson, W., "Rotor Airloads Prediction Using Loose Aerodynamic/Structural Coupling," *Journal of Aircraft*, Vol. 43, (3), 2006, pp. 732–742. DOI: 10.2514/1.14006.

4. Linton, D., Widjaja, R., and Thornber, B., "Actuator Surface Model with Computational-Fluid-Dynamics-Convected Wake Model for Rotorcraft Applications," *AIAA Journal*, Vol. 59, (8), 2021, pp. 2935–2949. DOI: 10.2514/1.J059952.

5. Steijl, R., and Barakos, G. N., "CFD Analysis of Complete Helicopter Configurations - Lessons Learnt From the GOAHEAD Project," *Aerospace Science and Technology*, Vol. 19, (1), 2012, pp. 58–71. DOI: 10.1016/j.ast.2011.01.007.

6. Lakshminarayan, V., Sitaraman, J., Roget, B., and Wissink, A., "Simulation of Complex Geometries Using Automatically Generated Strand Meshes," Paper AIAA 2018-0028, *Proceedings of the 2018 AIAA Aerospace Sciences Meeting*, Kissimmee, FL, 2018. DOI: 10.2514/6.2018-0028.

7. Meakin, R. L., Wissink, A. M., Chan, W. M., Pandya, S. A., and Sitaraman, J., "On Strand Grids for Complex Flows," Paper AIAA 2007-3834, *Proceedings of the 18th AIAA Computational Fluid Dynamics Conference*, Miami, FL, 2007. DOI: 10.2514/6.2007-3834.

8. Park, H. S., Linton, D., and Thornber, B., "Towards Detached-Eddy Simulation of Flow Around Rotorcraft Using Immersed Boundary Method," *AIAA Journal*, Vol. 58, (11), 2020, pp. 4893–4907. DOI: 10.2514/1.J059297.

9. Park, H. S., Linton, D., and Thornber, B., "Rotorcraft Fuselage and Ship Airwakes Simulations Using an Immersed Boundary Method,"

International Journal of Heat and Fluid Flow, Vol. 93, 2022, pp. 108916. DOI: 10.1016/j.ijheatfluidflow.2021.108916.

10. Park, J. H., Linton, D., and Thornber, B., "Simulation of Rotorcraft Fuselage with Rotor Effects Using an Immersed Boundary Method," *Journal of the American Helicopter Society*, Vol. 68, (2), 2023, pp. 59–70. DOI: 10.4050/JAHS.68.022006.

11. Linton, D., Barakos, G., Widjaja, R., and Thornber, B., "Coupling of an Unsteady Aerodynamics Model with a Computational Fluid Dynamics Solver," *AIAA Journal*, Vol. 56, (8), 2018, pp. 3153–3166. DOI: 10.2514/1.J056784.

12. Bousman, W. G., and Kufeld, R. M., "UH-60A Airloads Catalog," NASA TM 2005-212827, 2005.

13. Kufeld, R. M., Romander, E. A., Dominguez, M., and Dromiack, H., "UH-60A Airloads Flight Test Program: Data Counter 8513," NASA TM 2019-220317, 2019.

14. Kufeld, R. M., Romander, E. A., Dominguez, M., and Dromiack, H., "UH-60A Airloads Flight Test Program: Data Counter 8534," NASA TM 2019-220311, 2019.

15. Kufeld, R. M., Romander, E. A., Dominguez, M., and Dromiack, H., "UH-60A Airloads Flight Test Program: Data Counter 9017," NASA TM 2019-220310, 2019.

16. Biedron, R. T., and Lee-Rausch, E. M., "Computation of UH-60A Airloads Using CFD/CSD Coupling on Unstructured Meshes," *Proceedings of the 67th American Helicopter Society Annual Forum*, Virginia Beach, VA, 2011.

17. Lim, J. W., and Anastassiades, T., "Correlation of 2GCHAS Analysis with Experimental Data," *Journal of the American Helicopter Society*, Vol. 40, (4), 1995, pp. 18–33. DOI: 10.4050/JAHS.40.18.

18. Datta, A., and Chopra, I., "Validation and Understanding of UH-60A Vibratory Loads in Steady Level Flight," *Journal of the American Helicopter Society*, Vol. 49, (3), 2004, pp. 271–287. DOI: 10.4050/JAHS.49.271.

19. Steijl, R., Barakos, G. N., and Badcock, K. J., "Computational Study of the Advancing-Side Lift-Phase Problem," *Journal of Aircraft*, Vol. 45, (1), 2008, pp. 246–257. DOI: 10.2514/1.22044.

20. Datta, A., Sitaraman, J., Chopra, I., and Baeder, J. D., "CFD/CSD Prediction of Rotor Vibratory Loads in High-Speed Flight," *Journal of Aircraft*, Vol. 43, (6), 2006, pp. 1698–1709. DOI: 10.2514/1.18915.

21. Ananthan, S., Baeder, J. D., Sitaraman, J., Hahn, S., and Iaccarino, G., "Hybrid Unsteady Simulation of Helicopters: HUSH," Paper AIAA 2008-7339, *Proceedings of the 26th AIAA Applied Aerodynamics Conference*, Honolulu, HI, 2008. DOI: 10.2514/6.2008-7339.

22. Ahmad, J. U., and Chaderjian, N. M., "High-Order Accurate CFD/CSD Simulation of the UH-60 Rotor in Forward Flight," Paper AIAA 2011-3185, *Proceedings of the 29th AIAA Applied Aerodynamics Conference*, Honolulu, HI, 2011. DOI: 10.2514/6.2011-3185.

23. Ahmad, J., and Biedron, R. T., "Code-to-Code Comparison of CFD/CSD Simulation for a Helicopter Rotor in Forward Flight," Paper AIAA 2011-3819, *Proceedings of the 29th AIAA Applied Aerodynamics Conference*, Honolulu, HI, 2011. DOI: 10.2514/6.2011-3819.

24. Biedron, R. T., and Lee-Rausch, E. M., "An Examination of Unsteady Airloads on a UH-60A Rotor: Computation versus Measurement," *Proceedings of the 68th American Helicopter Society Annual Forum*, Fort Worth, TX, 2012.

25. Chaderjian, N. M., "Advances in Rotor Performance and Turbulent Wake Simulation Using DES and Adaptive Mesh Refinement," ICCFD7-3506, *Proceedings of the 7th International Conference on Computational Fluid Dynamics*, Big Island, HI, 2012.

26. Chaderjian, N. M., and Ahmad, J. U., "Detached Eddy Simulation of the UH-60 Rotor Wake Using Adaptive Mesh Refinement," *Proceedings of the 68th American Helicopter Society Annual Forum*, Fort Worth, TX, 2012.

27. Yeo, H., and Potsdam, M., "Rotor Structural Loads Analysis Using Coupled Computational Fluid Dynamics/Computational Structural Dynamics," *Journal of Aircraft*, Vol. 53, (1), 2016, pp. 87–105. DOI: 10.2514/1.C033194.

28. Chaderjian, N. M., "Navier-Stokes Simulation of UH-60A Rotor/Wake Interaction Using Adaptive Mesh Refinement," *Proceedings of the 73rd Annual AHS International Forum and Technology Display*, Fort Worth, TX, 2017.

29. Spalart, P. R., Deck, S., Shur, M. L., Squires, K. D., Strelets, M. Kh., and Travin, A., "A New Version of Detached-Eddy Simulation, Resistant to Ambiguous Grid Densities," *Theoretical and Computational Fluid Dynamics*, Vol. 20, 2006, pp. 181–195. DOI: 10.1007/s00162-006-0015-0.

30. Jasak, H., Rigler, D., and Tukovic, Z., "Design and Implementation of Immersed Boundary Method with Discrete Forcing Approach for Boundary Conditions," *Proceedings of the 6th European Conference on Computational Fluid Dynamics*, Barcelona, Spain, 2014.

31. Allmaras, S. R., Johnson, F. T., and Spalart, P. R., "Modifications and Clarifications for the Implementation of the Spalart-Allmaras Turbulence Model," ICCFD7-1902, *Proceedings of the 7th International Conference on Computational Fluid Dynamics*, Big Island, HI, 2012.

32. Tamaki, Y., Harada, M., and Imamura, T., "Near-Wall Modification of Spalart-Allmaras Turbulence Model for Immersed Boundary Method," *AIAA Journal*, Vol. 55, (9), 2017, pp. 3027–3039. DOI: 10.2514/1.J055824.

33. Beddoes, T. S., "Practical Computation of Unsteady Lift," *Vertica*, Vol. 8, (1), 1984, pp. 55–71.

34. Johnson, W., *Rotorcraft Aeromechanics*, Cambridge University Press, New York, NY, 2013.

35. Ramasamy, M., and Leishman, J. G., "A Reynolds Number-Based Blade Tip Vortex Model," *Journal of the American Helicopter Society*, Vol. 52, (3), 2007, pp. 214–223. DOI: 10.4050/JAHS.52.214.

36. Kim, T., Oh, S., and Yee, K., "Improved Actuator Surface Method for Wind Turbine Application," *Renewable Energy*, Vol. 76, 2015, pp. 16–26. DOI: 10.1016/j.renene.2014.11.002.

37. The OpenFOAM Foundation, "OpenFOAM Version 11," https://openfoam.org/ (accessed Aug. 1, 2023).

38. Spalart, P. R., Shur, M. L., Strelets, M. Kh., and Travin, A. K., "Sensitivity of Landing-Gear Noise Predictions by Large-Eddy Simulation to Numerics and Resolution," Paper AIAA 2012-1174, *Proceedings of the 50th AIAA Aerospace Sciences Meeting including the New Horizons Forum and Aerospace Exposition*, Nashville, TN, 2012. DOI: 10.2514/6.2012-1174.

39. Issa, R. I., "Solution of the Implicitly Discretised Fluid Flow Equations by Operator-Splitting," *Journal of Computational Physics*, Vol. 62, (1), 1986, pp. 40–65. DOI: 10.1016/0021-9991(86)90099-9.

40. Balch, D. T., Saccullo, A., and Sheehy, T. W., "Experimental Study of Main Rotor/Tail Rotor/Airframe Interactions in Hover - Volume I," NASA CR 166485, 1983.

41. Howlett, J. J., "UH-60A Black Hawk Engineering Simulation Program: Volume I - Mathematical Model," NASA CR 166309, 1981.

42. Hilbert, K. B., "A Mathematical Model of the UH-60 Helicopter," NASA TM 85890, 1984.

43. Bousman, W. G., "Aerodynamic Characteristics of SC1095 and SC1094 R8 Airfoils," NASA TP 2003-212265, 2003.

44. Lorber, P. F., Stauter, R. C., and Landgrebe, A. J., "A Comprehensive Hover Test of the Airloads and Airflow of an Extensively Instrumented Model Helicopter Rotor," *Proceedings of the American Helicopter Society's 45th Annual Forum*, Boston, MA, 1989.

45. Drela, M., "XFOIL: An Analysis and Design System for Low Reynolds Number Airfoils," *Low Reynolds Number Aerodynamics, Lecture Note in Engineering*, edited by T. J. Muller, Vol. 54, Springer, Berlin, Heidelberg, 1989, pp. 1–12. DOI: 10.1007/978-3-642-84010-4_1.

46. Viterna, L., and Corrigan, R., "Fixed Pitch Rotor Performance of Large Horizontal Axis Wind Turbines," *Large Horizontal Axis Wind Turbines: Proceedings of a Workshop*, Cleveland, OH, 1981.

47. Spalart, P. R., and Rumsey, C. R., "Effective Inflow Conditions for Turbulence Models in Aerodynamic Calculations," *AIAA Journal*, Vol. 45, (10), 2007, pp. 2544–2553. DOI: 10.2514/1.29373.